Ultrafast Exciton Transport at Early Times in Quantum Dot Solids

Zhilong Zhang[1], Jooyoung Sung[1,2*], Daniel T. W. Toolan[3], Sanyang Han[1], Raj Pandya[1,4], Michael P. Weir[5,6], James Xiao[1], Simon Dowland[1], Mengxia Liu[1], Anthony J. Ryan[3], Richard A. L. Jones[7], Shujuan Huang[8] and Akshay Rao[1*]

[1]Cavendish Laboratory, J.J. Thomson Avenue, University of Cambridge, Cambridge CB3 OHE, United Kingdom.

[2]Department of Emerging Materials Science, DGIST, Daegu 42988, Republic of Korea

[3]Department of Chemistry, The University of Sheffield, Sheffield S3 7HF, United Kingdom

[4]Laboratoire Kastler Brossel, École Normale Superiéure-Université PSL, CNRS, Sorbonne Université, College de France, Paris 75005, France

[5]Department of Physics and Astronomy, The University of Sheffield, Sheffield S3 7RH, United Kingdom

[6]School of Physics and Astronomy, The University of Nottingham, University Park, Nottingham NG7 2RD, United Kingdom

[7]Department of Materials Science, University of Manchester, Manchester M1 3BB, United Kingdom

[8]School of Engineering, Macquarie University, Sydney 2109, Australia

*email: ar525@cam.ac.uk, jooyoung@dgist.ac.kr

Quantum dot (QD) solids are an emerging platform for developing a range of optoelectronic devices. Thus, understanding exciton dynamics is essential towards developing and optimizing QD devices. Here, using transient absorption microscopy, we reveal the initial exciton dynamics in QDs with femtosecond timescales. We observe high exciton diffusivity (~10^2 cm^2s^{-1}) in lead chalcogenide QDs within the first few hundred femtoseconds after photoexcitation followed by a transition to a slower regime (10^{-1}~1 cm^2s^{-1}). QD solids with larger interdot distances exhibit higher initial diffusivity and a delayed transition to the slower regime, while higher QD packing density and heterogeneity accelerate this transition. The fast transport regime only occurs in materials with exciton Bohr radii much larger than the QD sizes, suggesting the transport of delocalized excitons in this regime and a transition to slower transport governed by exciton localization. These findings suggest routes to control the optoelectronic properties of QD solids.

Colloidal QDs have attracted great interest for fundamental studies of exciton and charge dynamics in semiconductor nanostructures, as well as for their applications in various devices including photodetectors[1], light emitting diodes (LEDs)[2], photovoltaics[3,4] and field effect transistors (FETs)[5]. Exciton transport in QD solids is generally believed to be determined by the packing structure of particles[1,2,6-9]. The requirement for exciton transport however differs between the applications, for example, a photovoltaic cell requires fast exciton transport to the charge-separating interfaces[3,4], whereas in a LED this can lead to undesired quenching of luminescence[2,6]. A comprehensive understanding of exciton transport physics in QD solids is therefore needed, with the eventual aim of controlling these transport properties in order to optimize device performance.

In comparison to the parallel issue of charge transport, the understanding of exciton transport in QD solids is less developed, partly due to limitations of experimental techniques. While FETs and Hall measurements under steady-state conditions provide a wealth of information on charge transport[5-7], excitons cannot be easily probed electrically in ensemble measurements. Coupled with their short-lifetime and diffusion lengths (compared to charges), the studies of exciton transport are limited to quenching or optical microscopy measurements. Time-resolved microscopy has been particularly powerful in probing exciton transport, especially at linking transport to the morphology of materials and probing time-dependent diffusion[10-15]. The general consensus that emerges from these studies is that closer packing of QDs enables faster exciton transport, while energetic/structural heterogeneity leads to reduction of diffusivity over time[11,13]. These conclusions together with the extracted diffusivities ($10^{-3} \sim 10^{-2}$ cm^2 s^{-1}) fit well within the picture of Förster resonance energy transfer (FRET) dominated hopping of localized excitons[14]. However, due to experimental limitations these studies have probed exciton transport in QD solids on pico/nano-second timescales following photoexcitation. As exciton behaviour is time-dependent, those conclusions can also be limited by the timescale measured.

Here we directly probe the initial exciton dynamics in QD solids in the femtosecond (fs) timescales following photo-generation. Surprisingly, we find that when the material has a Bohr radius much larger than the QD size, excitons first undergo very fast transport (diffusivity of $\sim 10^2$ cm^2 s^{-1}) within ~300 fs after photoexcitation and then switch into a much slower transport regime ($10^{-1} \sim 1$ cm^2 s^{-1}). Intriguingly, reducing the interdot distance in the QD solids only enhances transport in the slower regime, while it unexpectedly diminishes the initial fast regime.

Both QD packing density and heterogeneity have significant impacts on these transport regimes and the transition between them.

fs-TAM measurements on QD solids

Femtosecond transient absorption microscopy (fs-TAM) with 13 fs temporal resolution and 13-25 nm spatial precision is employed to monitor exciton transport in the QD films in this work (Fig. 1a, see Methods for full description). Briefly, a near diffraction-limited pump beam (effective width σ of 107 ± 7.5 nm) with transform-limited pulse duration (9.2 fs) is delivered onto the QD film, generating a Gaussian-shaped exciton density instantaneously. The spatial evolution of exciton distribution is recorded by imaging it with a loosely focused (σ of 6.4 μm) and transform-limited (6.8 fs) probe pulse at a series of variable time delays between pump and probe pulses (Supplementary Fig. S1-2). It should be noted that although spatial resolution is still limited by diffraction, by comparing subsequent TAM images it is possible to distinguish the changes in the shape of the distribution as small as 13-25 nm[16,17].

Lead sulfide (PbS) QDs (1.68 eV as-synthesized) were chosen as the main material platform in this work, as they are among the most intensively studied materials for QD-based devices due to the great optoelectronic performance[2,3,7]. A series of PbS QD solid-state films with systematic variation in the interdot spacing was prepared. This was achieved by solution-phase pre-exchange of the native oleic acid (OA) capping ligands arising from the synthesis to those with shorter carbon chains (Fig. 1b), namely dodecanoic acid (12C), octanoic acid (8C), hexanoic acid (6C) and butyric acid (4C) before film fabrication (Methods, Supplementary Fig. S3). Hereafter, the QD films are denoted as the corresponding ligands. Both the photoluminescence and excitonic features of the absorption spectra were maintained,

93 indicating successful ligand exchange without noticeable aggregation (Supplementary Fig. S4-
94 6).

95

96 Fig. 1c shows the conventional ensemble level transient absorption (TA) measurements of the
97 QD films (also Supplementary Fig. S7-11). A gradual red-shift of the photo-bleaching peak
98 feature can be seen when moving from QD films with OA to shorter ligands, which is consistent
99 with shorter interdot distance and hence stronger QD coupling[11,18]. There was only minor signal
100 decay within the measurement time window of fs-TAM (Supplementary Fig. S12 and
101 Supplementary Table. 1), suggesting very little recombination and hence this is unlikely to
102 affect the transport measurements. We also observe negligible time-dependent spectral red-
103 shift in the films within the timescale of fs-TAM measurements (Supplementary Fig. S7-11c),
104 implying the excitons experience a homogeneous energy landscape on the timescales being
105 probed in this work.

106

107 The fs-TAM images of each film were recorded at the probe wavelength corresponding to the
108 photo-bleaching peak feature (10 nm bandwidth, shaded areas in Fig. 1c). Representative fs-
109 TAM images obtained from OA are shown in Fig. 1d (Supplementary Fig. S13-16 for other
110 samples). The series of fs-TAM images clearly show spatial expansion of exciton distribution
111 in the QD film. Since the initial exciton distribution resembles the diffraction-limit pump beam
112 and the spatial expansion occurs isotropically, we fitted the fs-TAM images with an isotropic
113 two-dimensional Gaussian function and extracted the corresponding width, σ, as shown in Fig.
114 1e (also see Supplementary Fig. S17-20 for the fitting quality). Near time-zero, the initially
115 created exciton distribution gives a width of 172 ± 8 nm, which is similar to the that (180 nm)

calculated by convoluting diffraction-limited pump and probe beams[16]. By 260 fs this distribution expands to 224 ± 8 nm, clearly indicating exciton transport.

Two distinct exciton transport regimes

To quantitatively compare the transport dynamics in the QD solids, we employ the widely used mean squared displacement model (MSD = $\sigma_t^2 - \sigma_0^2$) to quantify the time-dependent variance of the spatial exciton distribution[10,11,16,17]. The MSD profiles of the films over time are plotted in Fig. 2a (Supplementary Fig. S21-22). We note that to account for spot-to-spot variations, the results for each sample presented were obtained from at least five different spots and averaged. The excitation density per QD, or $<N_{abs}>$ was kept at ~0.04, to create a similar excitation condition for all samples and to minimize higher order effects. Interestingly, two distinct transport regimes seem to exist in all MSD profiles: a very fast initial expansion of the exciton distribution within the first ~300 fs upon photoexcitation, followed by a much slower expansion (up to 4 ps time window). To test whether this is a two-step diffusion process or an anomalous diffusion process, we fitted the MSD evolution with the power law equation of MSD = $2Dt^{\alpha}$, where D is the diffusivity and α is the diffusion exponent[11,14,16,19]. We note that the MSD profiles cannot be fitted by a single equation, due to the abrupt transition between the two transport stages (Supplementary Discussion 1 and Fig. S23). Instead, the profiles can be well-fitted within separated time ranges for all samples. The fitting results of OA are shown in Fig. 2b as an example. Within the range of $t_0 < t < t_{fast}$, the dynamics can be well described by the power law equation where $\alpha = 1$, signifying that the initial exciton transport is diffusive[11,13,14,16,19]. The corresponding diffusivity (D_{fast}) can therefore be extracted from the slope of the fitted line. Similarly, for $t > t_{slow}$ the MSD profile can also be described by diffusive motion with a much smaller diffusivity (D_{slow}). A transition period (where $t_{fast} < t < t_{slow}$) exists

between the fast and slow diffusive stages (also see Supplementary Fig. S24-25). Alternatively, the slow diffusive stage can be described by a subdiffusive motion where $\alpha < 1$ (Supplementary Table. 2) by including the transition period (blue curve, Fig. 2b). We found that whether we take the description of diffusive or subdiffusive motion for the later slow transport the conclusion is consistent with that discussed below (Supplementary Discussion 2). We also note that the results are consistent when the pump fluence or repetition rate were modified, and signal expansion was not observed in samples containing diluted QDs in polymer matrices (Supplementary Fig. S26-31), hence the measurements were unlikely affected by Auger recombination, QD charging and systematic artefacts.

The extracted diffusivities from the fast and slow transport stages have opposite response to the reduction of ligand length in the QD solids (Fig. 2c). It has been generally believed that reducing the ligand length can lead to shorter interdot distance, hence improved QD coupling and transport[1,6,7]. Consistent with this general perception, the diffusivities in the slow regime increases with shorter ligands in the QD films (D_{slow}, red dots, Fig. 2c), apart from 4C (to be discussed below). The values of D_{slow} from 0.67 to 1.5 cm^2 s^{-1} were also comparable with exciton diffusivities reported in other QD systems[11,13], suggesting the slow stage is likely governed by a classical FRET hopping regime[14].

Intriguingly, the extracted diffusivities from the fast regime (D_{fast}) decrease with reducing ligand length, opposite to general perception of QD solids and the slow transport regime. The highest D_{fast} was obtained from OA (longest ligand), followed by 12C, 8C and 6C (black dots, Fig. 2c). 4C was again an exception, while its D_{fast} was higher than those with the medium-length ligands, however still lower than that of OA. Moreover, the values of the extracted D_{fast}

are within the range from 99 to 280 cm^2 s^{-1}, which is three to four orders of magnitude higher than those from D_{slow}.

We emphasize that the fs-time exciton transport in QD solids is revealed here experimentally for the first time. It has been well demonstrated that the exciton diffusivity of disordered material systems decrease over time[10-12,19], so high diffusivities in such an early-time range can be expected. Nevertheless, the observed D_{fast} values are obviously too high to be described by classical hopping in QDs, implying the fast regime is likely governed by a different mechanism. Interestingly, the estimated t_{fast} also shows the same trend as D_{fast} (black dots, Fig. 2d), indicating the films with longer ligands can sustain the initial fast transport for longer time. Similarly, the trend in t_{slow} also suggests longer ligands postpone the transition from the fast to the slow stage (red dots, Fig. 2d).

QD packing morphologies and exciton dynamics

Important questions then arise on the underlying mechanisms that dictate the two distinct transport regimes and why they have reversed trends of diffusivities when changing the ligand length. To further elucidate these, we looked into the quality and packing of the QD solids. We first compared the PLQY of the QD solids with those of the corresponding QD solutions (Fig. 3a). The PLQY of the QDs in solution were all around 35 ~ 40%, indicating they had similar level of surface defects. In contrast, the drop of PLQY when cast into films was more significant with shorter ligands, consistent with the expectation of better QD coupling and concomitant PL quenching[6,20]. We then performed grazing incidence small angle x-ray scattering (GISAXS) to reveal the actual interdot distance and packing heterogeneity (Fig. 3b and Supplementary Fig. S32). We found the average interdot distance (core-to-core) decreased

from ~37.2 Å for OA to ~31.5 Å for both 8C and 6C, whilst 4C maintained an unexpectedly large separation of ~35.5 Å (red dots, Fig. 3c, Supplementary Table. 3). The similar interdot distances between 8C and 6C (also diffusivities, Fig. 2c) can be attributed to the minor difference in ligand length and factors such as heterogeneity[21]. The QD packing disorder (FWHM of the peaks) gradually increased with shorter ligands (black dots, Fig. 3c). With this we attribute the unexpectedly large interdot distance of 4C to its high packing heterogeneity, which can lead to voids in the film (Supplementary Fig. S33). This can cause 4C to be an exception to the trend from Fig. 2c, as the diffusivities should vary based on the actual effective interdot distance of QDs instead of the absolute ligand length. We then correlate the diffusivities from Fig. 2c with the actual interdot distance of the films, and again confirm that D_{slow} increases with reduction of the actual interdot distance, while D_{fast} has the opposite trend (Fig. 3d).

In addition, the transition time between the two regimes is shorter in QD films with a higher level of packing disorder ($t_{trans} = t_{slow} - t_{fast}$, Fig. 3e), although it is difficult to decouple this from the effect of shorter interdot distance. Nevertheless, despite the fact that 4C has an average interdot distance between those of OA and 8C/6C, it has the shortest t_{trans} among all. For example, by comparing the MSD profiles of OA and 4C, it clearly suggests packing disorder accelerates the transition between the two transport regime (Fig. 3f).

The origin of the unusually fast exciton transport

Both the trend and values of D_{slow} are consistent with FRET hopping. In contrast, the values of D_{fast} and its trend with interdot distance are highly unusual. This transport phase is still diffusive in nature (as $\alpha = 1$), which seems to rule out ballistic ($\alpha = 2$) or coherent ($\alpha > 1$) motion [14,22,23].

One possible explanation is the transport of delocalized rather than localized excitons at early times[8,24] (see Supplementary Discussion 3 and 4). The range of interdot distances (31.5 Å~37.2 Å) should already allow decent coupling in lead chalcogenide QDs[7,25,26]. In addition, PbS has an exciton Bohr radius of 18 nm and the QDs studied here are 2.2 nm in diameter, so the highly confined regime may allow for large wavefunction leakage into neighbouring QDs[27-30].

To test the above hypothesis on exciton delocalization, we perform further fs-TAM measurements on cadmium chalcogenides (CdSe, CdS), cesium lead iodide ($CsPbI_3$) perovskite and lead selenide (PbSe) QDs. As shown in Fig. 4a-c, we observe no obvious growth in the MSD profiles of CdSe, CdS and $CsPbI_3$ QD solids with OA ligands. Interestingly, similar to PbS, PbSe QD solids also show the fast and slow transport regimes (Fig. 4d, also see Supplementary Discussion 3). We note that the exciton Bohr radii of lead chalcogenide QDs are very large, about 18 and 46 nm for PbS and PbSe, respectively[29], while those for cadmium chalcogenides and perovskites are only about 3-6 nm[31-33]. The exciton Bohr radius indicates the size of exciton and hence the potential extent of delocalization[34]. For cadmium chalcogenides and perovskite QDs, the largest possible ratio between the Bohr radius and typical particle radius (r_B/r_p) is about 1 to 4, without considering ligands (Supplementary Discussion 3). This implies very small possible exciton delocalization in these materials (Fig. 4e, small Bohr radius case), so with OA it cannot be supported. On the other hand, the r_B/r_p ratio for lead chalcogenides can be >15, when considering OA ligands in PbS it can still be around 10 (~18.6 Å effective radius). Therefore, a large delocalization extent can still be expected even with relatively large interdot distance (Fig. 4e large Bohr radius case, Supplementary Fig. S34). Based on this, we suggest that the fast transport regime observed here is based on the presence of exciton delocalization. Theoretical predictions suggest that delocalized excitons can transfer to sites that are energetically resonant but spatially far away

due to the enhanced net transition dipole moment from superposition of individual QD wavefunctions, leading to a 'supertransfer' mechanism (Supplementary Fig. S35)[35,36]. These delocalized excitons will eventually localize as they energetically relax and explore the density of states within the QD solid, leading to the transition to the hopping based slow regime. Further experimental and theoretical investigations are called for to investigate this phenomenon at early times, as the physics that drives this mechanism is generally not well captured within current models.

The important remaining question is why the initial fast transport is less efficient in QD solids when decreasing interdot distance (Fig. 3d). Here, we suggest one aspect of disorder that has been largely overlooked – the QD packing density that increases with shorter interdot distance (Supplementary Discussion 3). Conventional sources of disorder in QD solids include size polydispersity, surface defect states and packing heterogeneity[3,5,11]. But assuming the same polydispersity and defect level per QD, increasing the packing density would unavoidably increase the number of QDs in the transport path, potentially broadening the density of states explored by the excitons within the same distance. This problem is normally not noticeable for QDs with little delocalization, as the transport mechanism is most likely based on hopping of localized excitons, and short interdot distance is the most prior condition for any transport to occur (Fig. 4e). For lead chalcogenides where a large delocalization is already expected, reducing the distance further has very minor advantage to initial delocalization, but only increasing the number of QDs/disorder sites in the transport path (Fig. 4f-g). This would accelerate the transition to the hopping transport regime[30]. Similar observations have been made in carrier transport of organic semiconductors such as rubrene thin films, where the highest mobility was found in a packing direction with larger intermolecular distance[37,38].

Conclusion

With the above results, the early time exciton dynamics are summarized in Fig. 4f-g (also see Supplementary Fig. S36-37). Immediately after photoexcitation, delocalized excitons are generated in the QD solids studied here and diffuse quickly (fast transport). With larger (but still closely-packed) interdot distance and/or homogeneous packing (Fig. 4f), a low level of disorder allows faster transport and longer duration. However, when an exciton is eventually localized, the hopping transport is not efficient at such distances. With shorter interdot distance (Fig. 4g), the higher packing density can introduce more QDs (disordered sites) in the path. This promotes the localization process and limits the transport rate and duration. High packing heterogeneity can further accelerate the localization. However once the exciton is localized, it can still transport through the QDs relatively efficiently by hopping due to the short interdot separation, as one would normally expect in longer timescales.

In summary, our work has revealed the surprising early-time transport dynamics of excitons in QD solids. We observed the transition from a very fast to a slow regime over time. Since this is only found in QDs with large excitonic Bohr radii, we suggest these observations are related to the localization process of initially delocalized excitons. Counterintuitively, the initial regime was faster and sustained for longer in QD solids with larger interdot distance. We attribute this to disorder arising from higher QD packing density (hence disorder density) and structural heterogeneity that accelerate exciton localization, under the context that a large extent of delocalization exists. This study sheds light on the factors that dictate exciton transport in QD solids on fs timescales and provides design rules to engineer QD solids to tailor the desired transport properties in these systems on a range of timescales.

Acknowledgements

This work has received funding from the European Research Council (ERC) under the European Union's Horizon 2020 research and innovation programme (grant agreement number 758826). Z. Z. acknowledges funding from the European Union's Horizon 2020 research and innovation programme under the Marie Skłodowska-Curie Actions grant (No. 842271 – TRITON project). J.S. would like to acknowledge support from the DGIST Start-up Fund Program of the Ministry of Science and ICT(2022010005). D. T. W. T., M. P. W., A. J. R. and R. A. L. J. acknowledge support from the Engineering and Physical Sciences Research Council (UK) via grant EP/P027814/1. We thank Dr. David Paleček and Dr. Christoph Schnedermann (University of Cambridge) for the assistance with the TA spectroscopy measurements and for the useful discussion on transport dynamics. We also thank Dr. Yiming Wu (A*STAR Singapore) for the supports on figure preparations.

Author contributions

Z.Z., J.S. and A.R. conceived the project. Z.Z. performed the sample synthesis and fabrication. Z.Z. and J.S. performed fs-TAM and other optical measurements. D.T.W.T., M.P.W., A.J.R. and R.A.L.J. supported and performed the GISAXS measurements and analysis. SY.H and M.L. provided input into the sample preparation. J.X. conducted electron microscopy measurements. S.D. contributed to PLQY measurements. SJ.H. provided input to the design of experiments and discussion of results. Z.Z., J.S. and A.R. wrote the paper with input from all authors.

Correspondence and requests for materials should be addressed to J.S. or A.R.

Competing interests

The authors declare no competing interests.

Supplementary information

This file contains Supplementary Figures 1-37 and Supplementary Tables 1-4.

Figures

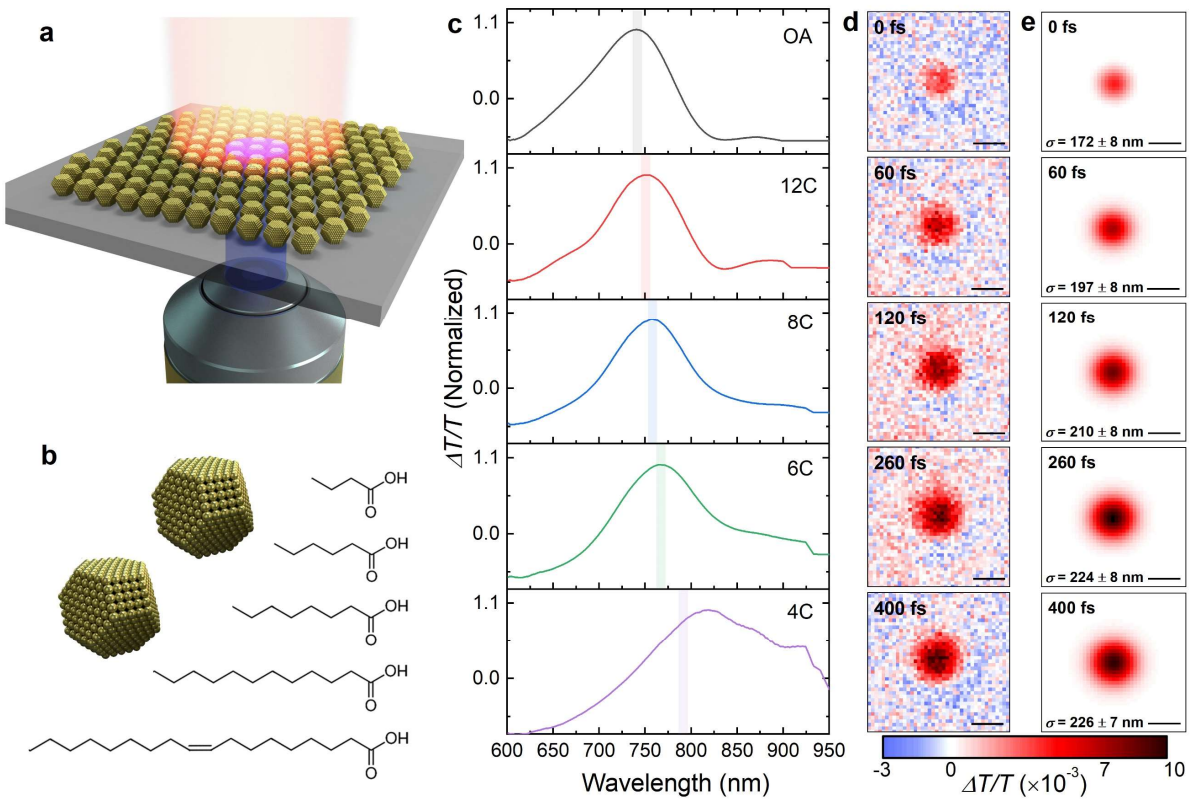

Fig. 1 fs-TAM measurement of QD thin films with different capping ligands. a, Schematic representation of the fs-TAM measurement. A near diffraction-limited (σ of 107 ± 7.5 nm) and transform-limited (9.2 fs, 580 nm) pump beam is delivered onto the QD film (blue beam), together with a counter-propagating loosely focused (σ of 6.4 μm) and transform-limited (6.8 fs) probe pulse (orange beam). Note that the actual samples are thicker films containing multiple layers of QDs with thicknesses of several hundred nm, and the QD packings contain certain levels of disorders. **b**, The interdot distance of the films were modified by the selection of surface ligands. The ligand exchange was performed to replace the original OA ligands to 12C, 8C, 6C or 4C ligands in solution-phase prior to film fabrication. **c**, Normalized TA spectra of the QD films with different ligands at 1 ps pump-probe time delay. Gradual red-shifts of the peaks were observed with shorter ligands. The fs-TAM data was taken near the corresponding positive $\Delta T/T$ photobleaching peaks with a

bandwidth of 10 nm (shaded area). **d**, Representative fs-TAM images of OA at 0, 60, 120, 260 and 400 fs pump-probe delay, respectively. The spectral bandwidth of 10 nm was achieved by using a bandpass filter (730 nm) in the imaging path. **e**, The corresponding exciton distribution images retrieved by fits with isotropic two-dimensional Gaussian functions. The σ values represent the width of exciton distribution at the corresponding time delay. Clear expansion of exciton distribution over time can be observed. The standard error represent 95% confidence intervals from the σ values obtained from five measurement spots on the sample. Scale bars, 500 nm.

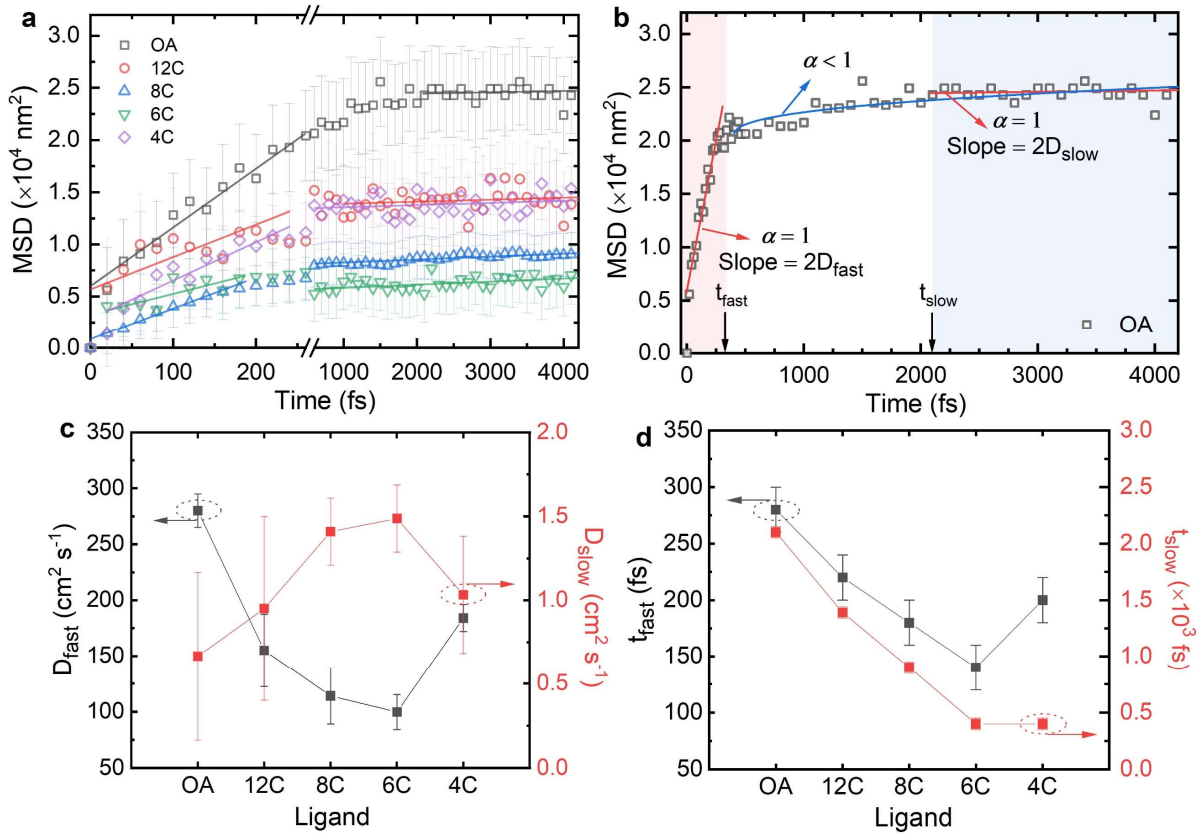

354

355 **Fig. 2 Quantitative fs-TAM measurement results of the series of QD thin films. a**, Time
356 evolution of the MSD = $\sigma_t^2 - \sigma_0^2$ profile, while σ_0^2 represents the variance of the spatial
357 exciton distribution near zero pump-probe delay. The error bars are standard error calculated
358 from those of σ over several measurement spots on the samples (see page 5 in Supplementary
359 Information for detailed calculation). The solid lines are the fits within the respective time
360 range based on the power law of MSD = $2Dt^{\alpha}$, where $\alpha = 1$. **b**, The fitted curves and
361 resultants parameters extracted for a representative QD film, OA as an example. The MSD
362 profile within the time range of $0 < t < t_{fast}$ and that of $t > t_{slow}$ can be well described by the
363 diffusive motion such that $\alpha = 1$ from the power law equation (red lines), where the
364 diffusivities of D_{fast} and D_{slow} can be extracted from the slope of the corresponding fitted
365 lines. The MSD profile after t_{fast} can also be described by a subdiffusive motion (blue curve,
366 $\alpha < 1$), while conclusions from the two fitting methods are consistent (Supplementary
367 Discussion 2). **c**, The extracted diffusivities of the initial fast transport regime (D_{fast}) and the

slow regime (D_{slow}) of the series of QD films. The two transport regimes show opposite response to the variation of ligands. **d**, The estimated time duration of the initial fast stage (t_{fast}) and the time taken (from 0 fs) for the excitons to enter the slow transport regime (t_{slow}). The error bars presented in **c-d** represent the uncertainty of the fitting parameters in the fitting process using the power law equation.

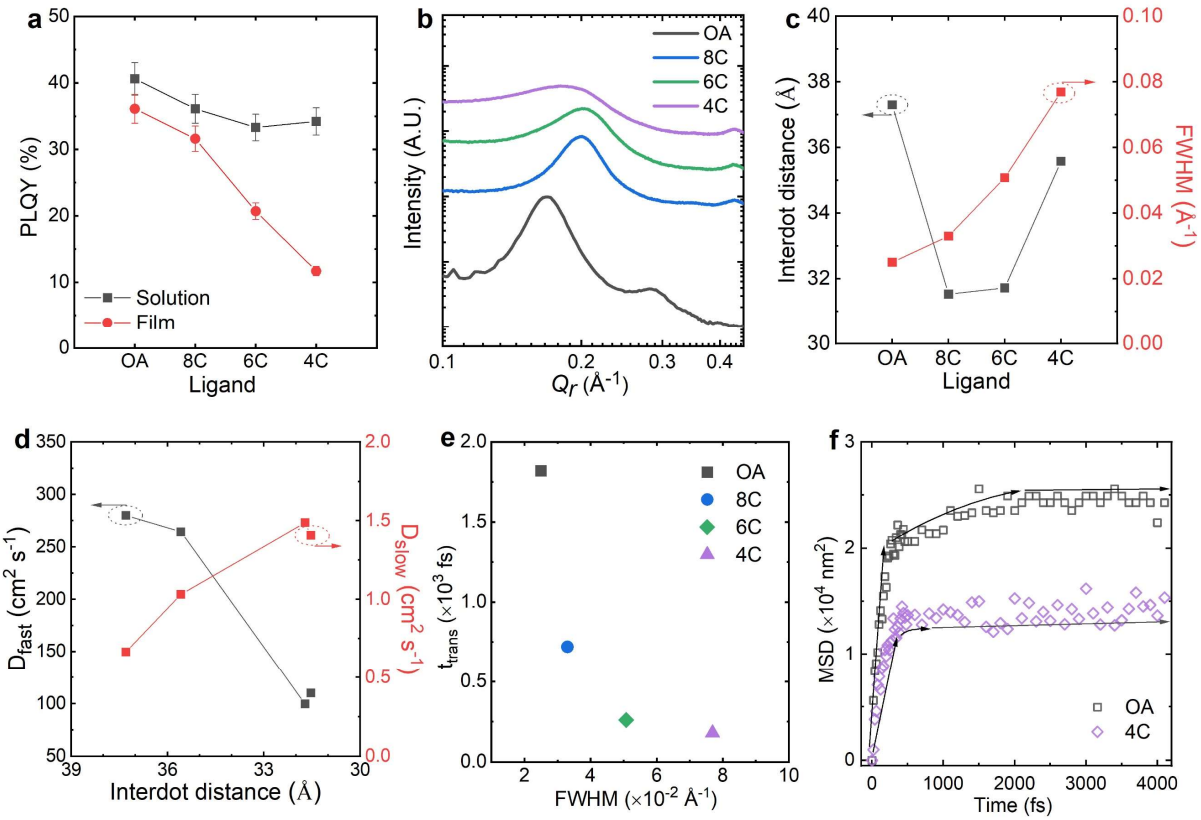

379

380 **Fig. 3 Quality and structural information of the QDs and films with different ligands**
381 **and correlation to the fs-TAM results. a**, PLQY of the QDs in both solution- and solid-
382 state with different ligands. A more significant quenching in the PLQY can be observed from
383 films with shorter ligands. No chemical or thermal treatment was applied to the films,
384 indicating that the quenching of PLQY arises from improved QD coupling due to closer
385 interdot distance. The error bars were calculated based on the system error of the PLQY set-
386 up (see Methods). **b**, Radially integrated GISAXS intensities of QD solids (normalized).
387 Lower Q_r value of the 1st order scattering peaks indicates larger average separation between
388 the QDs, while the peak width indicates discrepancy of the separation. **c**, The fitted interdot
389 distance and FWHM of the 1st order scattering peaks from **b**. We ascribe the FWHM to a
390 relative deviation in the core-to-core spacing of the QDs and hence level of packing disorder
391 in the samples. **d**, Correlation between the actual interdot distance (core-to-core) with the
392 diffusivities of the fast and slow regimes. The D_{fast} decreases with reducing interdot distance

while D_{slow} clearly shows an opposite trend. **e**, Correlation between the transition time (t_{trans} = $t_{slow} - t_{fast}$) with the FWHM (level of packing disorder) of the 1st order scattering peaks in **b**. The decreasing t_{trans} with increasing FWHM indicates higher level of disorder leads to faster transition from the fast to the slow regime. **f**, Comparison between the transition of transport regimes in OA and 4C, the arrows indicate the trend of MSD evolution.

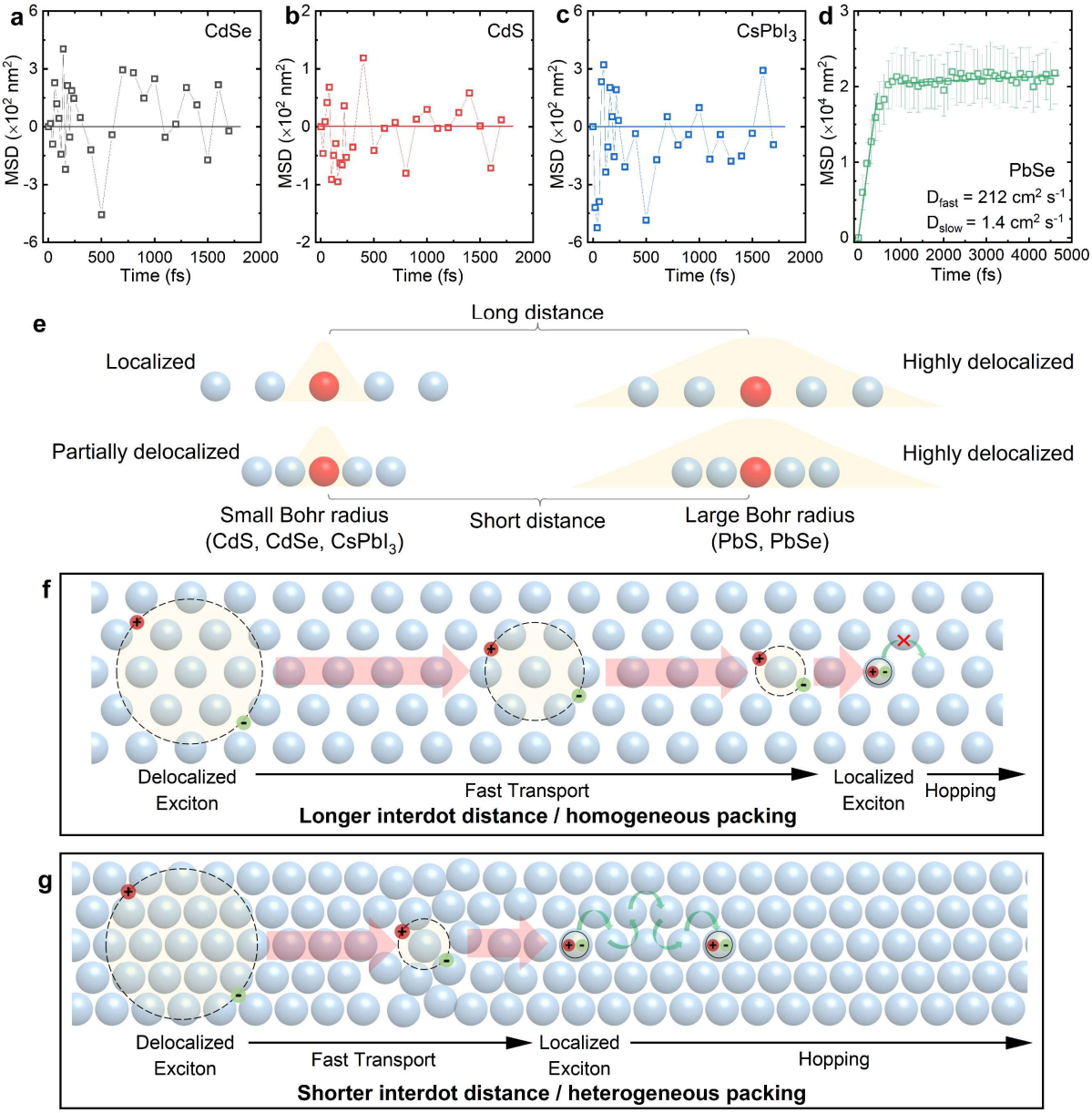

405

406 **Fig. 4 fs-TAM measurement results of other QD materials and schematics of exciton**
407 **delocalization in QD solids. a-c**, MSD profiles of CdSe, CdS and $CsPbI_3$ QD solids,
408 respectively. There is no exciton transport observed at early times. **d**, MSD profile of PbSe
409 QDs. Similar to PbS QDs, fast and slow transport regimes can clearly be observed, the
410 corresponding diffusivities are 212 and 1.4 $cm^2\ s^{-1}$, respectively. The error bars are standard
411 error calculated from those of σ over several measurement spots on the samples. **e**, Schematics
412 of exciton delocalization in QDs with small and large Bohr radius (wavefunction leakage).
413 With small Bohr radius the exciton delocalization is highly dependent on the interdot distance

(left), while that with large Bohr radius can still highly be delocalized even when the interdot distance is relatively large (right). **f**, Schematic of early-time exciton transport in QD solids with relatively long (but still closely-packed) interdot distance and/or homogeneous packing. **g**, Schematic of the case in QD solids with shorter interdot distance and/or heterogeneous packing. The excitons in both cases are likely delocalized initially, while the QD packing density and level of heterogeneity would affect the diffusivities and the localization process. Once the excitons are localized, the conventional hopping regime applies.

References

1. Lee, J. S., Kovalenko, M. V., Huang, J., Chung, D. S. & Talapin, D. V. Band-like transport, high electron mobility and high photoconductivity in all-inorganic nanocrystal arrays. *Nat. Nanotechnol.* **6,** 348-352. (2011)
2. Sun, L.*, et al.* Bright infrared quantum-dot light-emitting diodes through inter-dot spacing control. *Nat. Nanotechnol.* **7,** 369-373. (2012)
3. Liu, M.*, et al.* Hybrid organic-inorganic inks flatten the energy landscape in colloidal quantum dot solids. *Nat. Mater.* **16,** 258-263. (2017)
4. Chuang, C. H., Brown, P. R., Bulovic, V. & Bawendi, M. G. Improved performance and stability in quantum dot solar cells through band alignment engineering. *Nat. Mater.* **13,** 796-801. (2014)
5. Lan, X.*, et al.* Quantum dot solids showing state-resolved band-like transport. *Nat. Mater.* **19,** 323-329. (2020)
6. Kagan, C. R., Lifshitz, E., Sargent, E. H. & Talapin, D. V. Building devices from colloidal quantum dots. *Science* **353,** aac5523. (2016)
7. Kagan, C. R. & Murray, C. B. Charge transport in strongly coupled quantum dot solids. *Nat. Nanotechnol.* **10,** 1013-1026. (2015)
8. Crisp, R. W., Schrauben, J. N., Beard, M. C., Luther, J. M. & Johnson, J. C. Coherent exciton delocalization in strongly coupled quantum dot arrays. *Nano Lett.* **13,** 4862-4869. (2013)
9. Choi, J. H.*, et al.* Bandlike transport in strongly coupled and doped quantum dot solids: A route to high-performance thin-film electronics. *Nano Lett.* **12,** 2631-2638. (2012)
10. Akselrod, G. M.*, et al.* Visualization of exciton transport in ordered and disordered molecular solids. *Nat. Commun.* **5,** 3646. (2014)
11. Akselrod, G. M.*, et al.* Subdiffusive exciton transport in quantum dot solids. *Nano Lett.* **14,** 3556-3562. (2014)
12. Zhu, T., Wan, Y., Guo, Z., Johnson, J. & Huang, L. Two birds with one stone: Tailoring singlet fission for both triplet yield and exciton diffusion length. *Adv. Mater.* **28,** 7539-7547. (2016)

13. Yoon, S. J., Guo, Z., Dos Santos Claro, P. C., Shevchenko, E. V. & Huang, L. Direct imaging of long-range exciton transport in quantum dot superlattices by ultrafast microscopy. *ACS Nano* **10,** 7208-7215. (2016)
14. Ginsberg, N. S. & Tisdale, W. A. Spatially resolved photogenerated exciton and charge transport in emerging semiconductors. *Annu. Rev. Phys. Chem.* **71,** 1-30. (2020)
15. Delor, M., Weaver, H. L., Yu, Q. & Ginsberg, N. S. Imaging material functionality through three-dimensional nanoscale tracking of energy flow. *Nat. Mater.* **19,** 56-62. (2020)
16. Sung, J.*, et al.* Long-range ballistic propagation of carriers in methylammonium lead iodide perovskite thin films. *Nat. Phys.* **16,** 171-176. (2019)
17. Guo, Z., Manser, J. S., Wan, Y., Kamat, P. V. & Huang, L. Spatial and temporal imaging of long-range charge transport in perovskite thin films by ultrafast microscopy. *Nat. Commun.* **6,** 7471. (2015)
18. Choi, J. J.*, et al.* Photogenerated exciton dissociation in highly coupled lead salt nanocrystal assemblies. *Nano Lett.* **10,** 1805-1811. (2010)
19. Schnedermann, C.*, et al.* Ultrafast tracking of exciton and charge carrier transport in optoelectronic materials on the nanometer scale. *J. Phys. Chem. Lett.* **10,** 6727-6733. (2019)
20. Zhang, J.*, et al.* Carrier transport in pbs and pbse qd films measured by photoluminescence quenching. *J. Phys. Chem. C* **118,** 16228-16235. (2014)
21. Weidman, M. C., Yager, K. G. & Tisdale, W. A. Interparticle spacing and structural ordering in superlattice pbs nanocrystal solids undergoing ligand exchange. *Chem. Mater.* **27,** 474-482. (2014)
22. Contreras-Pulido, L. D. & Bruderer, M. Coherent and incoherent charge transport in linear triple quantum dots. *J. Phys. Condens. Matter.* **29,** 185301. (2017)
23. Barford, W. & Duffy, C. D. P. Role of quantum coherence and energetic disorder in exciton transport in polymer films. *Phys. Rev. B* **74,** 075207. (2006)
24. Cohen, E.*, et al.* Achieving exciton delocalization in quantum dot aggregates using organic linker molecules. *J. Phys. Chem. Lett.* **8,** 1014-1018. (2017)
25. Geiregat, P., Justo, Y., Abe, S., Flamee, S. & Hens, Z. Giant and broad-band absorption enhancement in colloidal quantum dot monolayers through dipolar coupling. *ACS Nano* **7,** 987-993. (2013)
26. Kagan, C. R., Murray, C. B., Nirmal, M. & Bawendi, M. G. Electronic energy transfer in cdse quantum dot solids. *Phys. Rev. Lett.* **76,** 1517-1520. (1996)
27. He, S.*, et al.* Engineering sensitized photon upconversion efficiency via nanocrystal wavefunction and molecular geometry. *Angew. Chem. Int. Ed. Engl.* **59,** 17726-17731. (2020)
28. Koole, R., Liljeroth, P., de Mello Donega, C., Vanmaekelbergh, D. & Meijerink, A. Electronic coupling and exciton energy transfer in cdte quantum-dot molecules. *J. Am. Chem. Soc.* **128,** 10436-10441. (2006)
29. Ma, W., Luther, J. M., Zheng, H., Wu, Y. & Alivisatos, A. P. Photovoltaic devices employing ternary pbsxse1-x nanocrystals. *Nano Lett.* **9,** 1699-1703. (2009)
30. Collini, E.*, et al.* Room-temperature inter-dot coherent dynamics in multilayer quantum dot materials. *J. Phys. Chem. C* **124,** 16222-16231. (2020)
31. Razgoniaeva, N.*, et al.* One-dimensional carrier confinement in "giant" cds/cdse excitonic nanoshells. *J. Am. Chem. Soc.* **139,** 7815-7822. (2017)

32. Jethi, L., Mack, T. G. & Kambhampati, P. Extending semiconductor nanocrystals from the quantum dot regime to the molecular cluster regime. *J. Phys. Chem. C* **121,** 26102-26107. (2017)
33. Protesescu, L.*, et al.* Nanocrystals of cesium lead halide perovskites (cspbx(3), x = cl, br, and i): Novel optoelectronic materials showing bright emission with wide color gamut. *Nano Lett.* **15,** 3692-3696. (2015)
34. Wise, F. W. Lead salt quantum dots: The limit of strong quantum confinement. *Acc. Chem. Res.* **33,** 773-780. (2000)
35. Lee, E. M. Y., Tisdale, W. A. & Willard, A. P. Perspective: Nonequilibrium dynamics of localized and delocalized excitons in colloidal quantum dot solids. *J. Vac. Sci. Technol. A* **36,** 068501. (2018)
36. Sharma, A.*, et al.* Supertransport of excitons in atomically thin organic semiconductors at the 2d quantum limit. *Light Sci. Appl.* **9,** 116. (2020)
37. Fratini, S., Nikolka, M., Salleo, A., Schweicher, G. & Sirringhaus, H. Charge transport in high-mobility conjugated polymers and molecular semiconductors. *Nat. Mater.* **19,** 491-502. (2020)
38. Schweicher, G.*, et al.* Chasing the "killer" phonon mode for the rational design of low-disorder, high-mobility molecular semiconductors. *Adv. Mater.* **31,** 1902407. (2019)

Methods

Sample preparation

Synthesis of PbS QDs. The synthesis of PbS QDs was carried out following modified versions of previously reported methods[39]. Briefly, lead oxide (0.45 g), oleic acid (1.4 g) and 1-octadecene (10 g) were loaded in a three-neck flask and degassed at 110 °C for 2 h. Subsequently, the reaction flask was flushed with nitrogen and the temperature was lowered to 50 °C. A solution containing bis(trimethylsilyl)sulfide (210 μL) in 1-octadecene (5 mL) was rapidly injected into the lead precursor solution. After 2 min, the reaction flask was cooled down to ambient temperature (~25 °C) with a water bath. The PbS QDs were first extracted by adding hexane and acetone, followed by centrifugation. The QDs were further purified three times with hexane and acetone. After purification, the QDs were re-dispersed in toluene at a concentration of 50 mg mL^{-1} and stored in a nitrogen filled glovebox. Before ligand exchange, the dispersion was filtered with a 0.45 um PTFE syringe filter to remove residual impurities.

Ligand exchange. The ligand exchange of QDs were performed according to literature with some modifications[40]. In a nitrogen filled glovebox, the purified QDs (50 mg mL^{-1} in toluene) were first loaded into separated sample vials and kept under magnetic stirring. The liquid phase ligands (8C, 6C and 4C) were slowly added into the QD dispersion by using a micropipette. Typically ~ 0.1 mmol of ligands are added to 100 mg of QDs. As the 12C ligand is solid-state, it was first dissolved in toluene (~50 mg mL^{-1}) before being added into the QD dispersion. After the ligands were added, the QD dispersions were further stirred for about 30 min. The exchanged QDs were purified by adding extra toluene and acetonitrile, followed by centrifugation. The purification process was repeated by another twice to remove

residual ligands. The purified QDs were then dispersed in hexane at a concentration of ~50 mg mL^{-1} and filtered. The hexane solvent is then removed by vacuum-drying and the QDs were finally dispersed in toluene at a concentration of 300 mg mL^{-1} (based on the initial amount for exchange). Note that the QDs with OA ligands (the QD stocks without ligand exchange) were also further purified three times with toluene and acetonitrile to keep consistency of the purification conditions over all samples.

Film sample fabrication. All QD film samples were deposited on high precision microscope cover glasses (purchased from Marienfeld Superior) with the size of 18 × 18 mm and thickness No. 1.5H (170 ± 5 μm). The substrates were handled with extra care as they are very thin and fragile. The substrates were cleaned subsequently by mild sonication with detergent, isopropanol, acetone and deionized water followed by drying with a nitrogen gun. The deposition of QD films were performed inside a nitrogen filled glovebox. Typically, 50 μL of the QD dispersion was dispensed on the substrate and then spin-dried at 1500 rpm for 1 min. The film samples were stored inside the glovebox overnight to allow the solvent to fully evaporate. The samples were encapsulated inside the glovebox before any optical measurements, and we found that a good encapsulation was the key to a successful fs-TAM measurement as the pump and probe pulse lasers were focused on very small areas on the samples. Air leakage caused the samples to quickly degrade (which appears as a 'burnt' hole on the film as observed by the microscope) or very inconsistent results from spot to spot on the same sample. To encapsulate a sample, the QDs deposited near the edges of the substrate were first removed by a cotton stick wetted with hexane. Another coverslip was then place onto the substrate (with some carbon tapes to fix the position), and the edges were sealed with epoxy. A schematic of a typical finished sample are shown in Supplementary Fig. S3.

Characterizations

UV-Vis-NIR absorption measurement. The absorption spectra of the samples were measured using a Shimadzu UV-3600 Plus. The solution samples were measured (inside a quartz cuvette) together with a reference sample with neat solvent. For film samples, an integrated sphere was used to minimize scattering effects.

Photoluminescence quantum yield. PLQY measurements were made following the procedure of a previous study[41]. Temperature and current controlled laser diodes (Thorlabs) were used to generate stable laser beams (520 nm). These were focused through a small hole onto samples suspended in a Spectralon coated integrating sphere (Newport 819C-SL-5.3) modified with a custom baffle extension. Light from the experiment was collected using an optical fibre connected to an Andor Kymera 328i Spectrometer housing a DU490A-1.7 InGaAs detector. The system was calibrated with a reference lamp (Ocean Optics) prior to the measurement.

Transmission electron microscope (TEM). Transmission electron microscopy was performed using a FEI Tecnai F20 TEM at 200kV accelerating voltage and imaged with a Gatan Orius SC1000 CCD camera. Samples of dilute QD solutions (<0.1 mg mL^{-1}) were dropcast from toluene onto 200-mesh carbon-coated Cu grids (Agar AGS160).

Femtosecond transient absorption spectroscopy. An amplified diode Yb:KGW laser system (Pharos, Light Conversion) at 38 kHz repetition rate provided ~180 fs pulses at 1030 nm. White light continuum (WLC) probe was generated in 4 mm YAG crystal and two 90° off-axis parabolic mirrors were used to recollimate and focus the WLC to ~100x100 μm spot on the sample. Other part of the fundamental was used to generate a third harmonic (453 nm, HIRO, Light Conversion) to amplify another WLC generated in 3 mm sapphire via non-collinear optical parametric amplification (NOPA) process in type I BBO crystal. The NOPA

591 output was centred at 540 nm, and then pre-compressed to ~15 fs using chirped mirrors and
592 fused silica wedges. After that, pump beam was delayed in respect to the probe beam by a
593 translation stage (Thorlabs, DDSM100/M) and focused to 545x360 μm spot-size on the
594 sample by a spherical mirror.

595 A sequence of probe pulses with and without the pump was generated by mechanical
596 chopping of the pump at 9.5 kHz. Transmitted probe beam through the sample was split with
597 a 950 nm dichroic mirror (Thorlabs). The visible part was imaged with a Silicon photodiode
598 array camera (Stresing Entwicklunsbüro) after dispersing it in a visible spectrograph (550 nm
599 blazed grating). The near-infrared portion of the probe was dispersed in an IR spectrograph
600 (1200 nm blazed grating) and imaged on an InGaAs photodiode array camera (Sensors
601 Unlimited). Data acquisition was shot-to-shot in respect to the chopper frequency. Offsets
602 due to the differing spectral response of the detectors was accounted for in the post-
603 processing of data.

604 **Femtosecond transient absorption microscopy (fs-TAM).** A Yb:KGW laser system
605 (Pharos, Light Conversion) provided 200 fs, 30 μJ pulses at 1030 nm with 200 kHz repetition
606 rate. The output fundamental beam was divided by a beam splitter and seeded two broadband
607 white light continuum (WLC) stages. The probe WLC was generated in a 3 mm YAG crystal
608 and adjusted to cover the wavelength range from 650-950 nm by a fused-silica prism-based
609 spectral filter. The pump WLC was generated in a 3 mm sapphire crystal to achieve bluer
610 WLC to 500 nm. The red-edge of pump beam is selected by 650 nm short-pass filter
611 (Thorlabs, FESH650). A set of chirped mirrors (pump; 109811, Layertec, probe; DCM9,
612 Venteon) and a pair of fused silica wedges (Layertec) compressed the pulses to 9.2 fs (pump)
613 and 6.8 fs (probe), as verified by second-harmonic generation frequency-resolved optical
614 gating (SHG-FROG) (see Pulse characterization, Supplementary Fig. S2). The pump pulse
615 was further pre-compressed with another set of chirped mirrors (109811, Layertec) to

compensate the dispersion in the microscope optics. The corresponding cross-correlation curve simulated with the retrieved pump and probe temporal profiles given in Supplementary Fig. S2 reveals an effective time resolution of 13 fs. A mechanical translation stage (Newport, CONEX-AG-LS25-27P) was used to delay the probe with respect to the pump. A clean TEM00 mode for pump was achieved with a pinhole and was collimated to completely fill the aperture of objective lens. The pump beam was then focused onto the sample by an oil immersion objective (100x, effective NA of 1.1) to the near diffraction limited spot (ca. 263 nm (FWHM) and 111 nm (width)) while the probe pulse was delivered into the sample with the relatively large focal spot (ca. 15 μm) from the opposite direction. The transmitted probe pulse was collected by the same objective and sent to an EMCCD camera (QImaging, RoleraTM Thunder). The total magnification of the imaging system was 288x. The scattered pump light was rejected by a 650 nm long-pass filter (Thorlabs, FEL650) inserted in front of the camera. Differential imaging was achieved by modulating the pump beam at 30 Hz by a mechanical chopper. We applied no gain to the EMCCD camera during the measurements. Moreover, fs-TAM images were obtained by averaging images taken over 50 runs at 5 different spots of each films.

The probing wavelengths were selected (using a bandpass filter with 10 nm width) according to the photo-bleaching peak position of the corresponding samples, as shown in the TA results. The wavelengths are 740 nm for OA, 750 nm for both 12C and 8C, 770 nm for 6C and 780 nm for 4C.

Grazing incidence Small angle scattering (GISAXS) measurement. GISAXS was performed on the Xuess instrument equipped with an Excillum MetalJet liquid gallium X-ray source. Alignment was performed on silicon substrates via three iterative height (z) and rocking curve (Ω) scans, with the final grazing incidence angle set to Ω = 0.2º. Scattering patterns were recorded on a vertically-offset Pilatus 1M detector with a sample to detector

distance of either 332 or 553 mm, calibrated using a silver behenate standard to achieve a q-range of 0.045 – 2.0 $Å^{-1}$. Two-dimensional images were recorded with exposure time of 600 s. The images were masked to remove the sample horizon, detector module gaps and beamstop and radially integrated from the apparent beam centre. Data correction and reduction was performed using the GIXSGUI MATLAB toolbox[42]. Two-dimensional scattering data was reduced to one-dimensional via radial integration, which was performed with a mask to remove contributions from "hot pixels", the substrate horizon and reflected beam. The core-to-core spacing and FWHM were obtained by fitting a Gaussian to the scattering peaks.

Data availability

The data underlying all figures in this article is publicly available from the University of Cambridge repository at https://doi.org/10.17863/CAM.80070.

References

39. Hines, M. A. & Scholes, G. D. Colloidal pbs nanocrystals with size-tunable near-infrared emission: Observation of post-synthesis self-narrowing of the particle size distribution. *Adv. Mater.* **15,** 1844-1849. (2003)
40. Nienhaus, L.*, et al.* Speed limit for triplet-exciton transfer in solid-state pbs nanocrystal-sensitized photon upconversion. *ACS Nano* **11,** 7848-7857. (2017)
41. de Mello, J. C., Wittmann, H. F. & Friend, R. H. An improved experimental determination of external photoluminescence quantum efficiency. *Adv. Mater.* **9,** 230-232. (1997)
42. Jiang, Z. Gixsgui: A matlab toolbox for grazing-incidence x-ray scattering data visualization and reduction, and indexing of buried three-dimensional periodic nanostructured films. *J. Appl. Crystallogr.* **48,** 917-926. (2015)